



RESEARCH ARTICLE

Chemical identification of microfossils from the 1.88-Ga Gunflint chert: Towards empirical biosignatures using laser ablation ionization mass spectrometer

Rustam A. Lukmanov¹  | Marek Tulej¹ | Niels F. W. Ligterink¹ |
Coenraad De Koning¹ | Andreas Riedo¹  | Valentine Grimaudo¹ |
Anna Neubeck² | David Wacey³ | Peter Wurz¹

¹Space Research & Planetary Sciences (WP), University of Bern, Bern, Switzerland

²Department of Earth Sciences, Uppsala University, Uppsala, Sweden

³Centre for Microscopy, Characterisation and Analysis, The University of Western Australia, Perth, Western Australia, Australia

Correspondence

Rustam A. Lukmanov, Space Research & Planetary Sciences (WP), University of Bern, Bern, Switzerland.
Email: rustam.lukmanov@space.unibe.ch

Funding information

Australian Research Council; Swiss National Science Foundation

Abstract

In this contribution, we investigated the chemical composition of Precambrian microfossils from the Gunflint chert (1.88 Ga) using a miniature laser ablation ionization mass spectrometer (LIMS) developed for in situ space applications. Spatially resolved mass spectrometric imaging (MSI) and depth profiling resulted in the acquisition of 68,500 mass spectra. Using single mass unit spectral decomposition and multivariate data analysis techniques, we identified the location of aggregations of microfossils and surrounding inorganic host mineral. Our results show that microfossils have unique chemical compositions that can be distinguished from the inorganic chert with high fidelity. Chemical depth profiling results also show that with LIMS microprobe data, it is possible to identify chemical differences between individual microfossils, thereby providing new insights about nature of early life. Analysis of LIMS spectra acquired from the individual microfossils reveals complex mineralization, which can reflect the metabolic diversity of the Gunflint microbiome. An intensity-based machine learning model trained on LIMS Gunflint data might be applied for the future investigations of putative microfossils from silicified matrices, where morphological integrity of investigated structures is lost, and potentially in the investigation of rocks acquired from the Martian surface.

KEYWORDS

Gunflint, Mars, mass spectrometry, microfossils, space instrumentation

1 | INTRODUCTION

In situ research and remote sensing have provided multiple lines of evidence that clement conditions were present on the surface of early Mars.^{1–3} Moreover, recent radar studies reveal evidence of subglacial liquid water on Mars,⁴ which supports the hypothesis that microbial life forms (extinct or extant) may be preserved within the Martian subsurface.^{4,5}

This is an open access article under the terms of the Creative Commons Attribution License, which permits use, distribution and reproduction in any medium, provided the original work is properly cited.

© 2021 The Authors. *Journal of Chemometrics* published by John Wiley & Sons Ltd.

All these observations provide a strong rationale for the search of biosignatures on the Red Planet. The current state of space exploration provides foundation for new measurement techniques and novel analytical approaches⁶ to identify and characterize minerals and potential signatures of life, if any, on Mars. However, in situ investigation of rocks on Mars faces multiple technological difficulties, ranging from constraints on instrumentation robustness, size, and power consumption to the quality of the acquired data.⁷ Some authors proposed an implementation of multicriteria approach^{3,8,9} to confirm or reject a biogenic origin of the given sample. Multicriteria approach, thus, requires several instruments onboard of the rover providing a multiplex analysis of the same sample and identification of morphological, molecular, elemental, and isotopic signatures of life. However, traditional methods used in space research, for example, bulk analysis and remote sensing instrumentation, might not be sufficiently sensitive to detect faint features from micrometer-sized (and below) organic material or microbial remains^{6,10} and, in some cases, can alter the chemistry of the sample. There is a growing demand for sensitive, in situ instruments with high spatial resolution and minimal sample processing, providing elemental and organic composition detection, which will enhance the scientific return from the missions to Mars and icy moons of Jupiter.^{6,10–12}

In addition to the development of analytical methods, development of chemometric tools has also proven to be a field of high importance to the current and future space exploration programs.¹³ For example, multivariate curve resolution alternating least squares have been shown to successfully identify various minerals and compounds from Raman hyperspectral images, overcoming the spectral overlap issues.^{14,15} The linear mixture model (LMM) was successfully used to quantify the abundance of major elements using the laser-induced breakdown spectroscopy (LIBS) spectra.¹⁶ Furthermore, a data fusion approach was reported for complementary analytical techniques (Raman and LIBS) that improved the classification limits of investigated binary compounds.¹⁷

Laser-based mass spectrometry is an emerging and sensitive technique that has shown to be capable of measuring extremely low concentrations (fmol) of amino acids in desorption mode,¹⁸ elemental detection of single microbes in Martian mudstone analog material,¹¹ and provides chemical (element, isotope) analysis in ablation mode of any solid material. The latter can be conducted with a depth resolution on the scale of tens of nm^{19,20} and with high element detection sensitivity down to the ppb level.^{21,22} This makes laser-based mass spectrometry an attractive method in the field of in situ chemical analysis on planetary surfaces.²³ The upcoming ExoMars mission/Rosalind Franklin Rover contains a Laser Desorption/Ionization (LDI)-Quadrupole Mass Spectrometer in its instrument suite,^{24,25} stimulating further development of LDI instruments.^{26–30} However, laser ablation ionization mass spectrometer (LIMS) capability to detect and identify billion-year-old microfossils has not been shown so far.

Since the discovery of Precambrian microbial communities in the 1.88-Ga Gunflint Formation (Ontario, Canada) in the early 1960s,^{31–33} many more examples of Precambrian life have been found, but the Gunflint Formation retains its place as a premier Precambrian Fossil-Lagerstätten, demonstrating that Paleoproterozoic life was widespread, already complex, and diversified.^{12,34,35} The Gunflint chert sample in this study has been used as a Martian analog, reflecting the iron-rich nature of the Martian sediments, as well as taking into account that siliceous sediments have high preservation capacity and are of interest to upcoming astrobiological missions.^{34,36–38} However, despite being among the best example of Precambrian life, phylogenetic affinities and metabolic speciation of the Gunflint microfossils remain largely unknown. Similarly, microfossils of unknown affinities dominate the majority of the Precambrian record.³⁹ Traditionally, the classification of types of microfossils has relied on morphological features^{31,40} and later advanced to include isotope fractionation⁴¹ and multielement nano-characterization of individual microfossils.³⁵ However, within the space instrumentation domain, detection of individual microfossils remains a technological challenge.¹⁰

In this contribution, we present results on mass spectrometric imaging (MSI) and chemical depth profiling from the Gunflint chert using a miniature time-of-flight reflectron-type mass spectrometer developed for in situ space applications, equipped with a femtosecond (fs) UV-258-nm laser ablation ion source. Mass spectrometric studies conducted on microfossils allowed their identification within the inorganic host material. Utilizing the depth profiling approach, we removed the contaminated layer present on the rock surface and probed the original chemical composition of the microfossils. The network-based approach used for the interpretation of hundreds of recorded mass spectra revealed a new topological dimension, where separate mineralogical inclusions present within the same analytical spot (inclusions smaller than the size of the ablation spot) can be readily separated.

The analysis of the mass spectra from the depth profiles revealed the presence of major biorelevant elements (CHNOPS), microscopic inclusions of Cu, Cr sulfides, rare earth element (REE) minerals in addition to the majority of Fe-dominated mineralization associated with the microfossils. These observations can indicate the presence of sulfur-processing and iron-processing species⁴² but also can indicate the presence of intracellular biomineralization machinery

(passive mineralization) within the Gunflint microbiome to withstand possible Cr and Cu toxicity within an already highly ferruginous environment.³⁹ H/C, O/C, Si/C ratios, and principal component analysis (PCA) scores calculated from the depth profiling dataset show ratios and intensity regions in which microfossils can be identified. Large-scale mass spectra sampling allowed the construction of binary classification machine learning (ML) models, which can be used for the identification of microfossils from other Precambrian cherts and other rocks (once calibrated), where morphological integrity of the putative microfossils is lost, thus providing a way to assess biogenicity, by comparing spectra from other cherts to our truly biogenic model data.

Overall, the LIMS microprobe shows an ability to identify micro- and nano-mineralization associated with the microfossils. LIMS imaging combined with accurate depth profiling has the potential to reveal new insights into the distribution, preservation, and elemental speciation of microfossils from Precambrian cherts and a potential to deliver insights into the chemical composition of samples acquired from the Martian surface.

2 | MATERIALS AND METHODS

A standard double-polished thin section of the Gunflint chert (collected from the Schreiber beach locality, Ontario, Canada) with a thickness of ~ 30 μm was used in the current study. The sample was mounted on a metal sample holder with vacuum-compatible copper tapes to fix the sample on the surface of the steel holder. No additional treatment of the sample was performed. A miniature time-of-flight mass spectrometer (TOF-MS) developed at the University of Bern has been used to study the Gunflint sample. The mass analyzer has small dimensions: $\text{O} 60 \text{ mm} \times 160 \text{ mm}$, which makes it suitable for space exploration programs as part of the lander or rover.^{7,23,30} The time-of-flight mass analyzer works in the positive ion detection mode and provides a single unit mass resolution and a ppm-level sensitivity. For the detailed characterization of the instrument and method in general, we refer the interested reader to the reviews^{43,44} and technical reports describing figures of merit.^{21,23,45,46} In the current laboratory setup, a mass spectrometer is accompanied by an integrated microscopy system¹² and a fs UV-258-nm ionization source. The instrument is designed to have spatial molecular,^{18,47} elemental, and isotopic^{22,29} mapping capabilities of solid samples. The microscopy system utilized in the current laboratory environment is not space qualified; however, a separate space prototype was developed in our group that combines the microscopy system, mass analyzer, and an ion source.²³ High precision XYZ translation stage is used for the accurate sample positioning under the instrument: 1- μm positioning accuracy is typically achieved between the internal microscope and laser focal point positions.¹² Laser power output stability, beam profile, and crater shapes are checked prior to the measurement campaign.

The Gunflint sample studied in this work could be approximated as a dielectric glass with inclusions of dark absorptive features (microfossils). To enhance the ionization efficiency of the quartz mineral, which constitutes most of the sample, and shorten the gap between the ionization efficiency of microfossils and host mineral, we implemented a frequency tripling system (STORC) into the beam delivery line, which allowed us to reach a stable fs UV-258-nm laser radiation. Photon energy, at this point, reached 4.8 eV, which is well suited for the ablation and ionization of any solid materials. Ti:sapphire fs Laser from Clark Inc. generates infrared (IR) 775-nm fundamental wavelength (180 fs), which is guided into the frequency doubling and tripling system. β -BBO crystals are used in the doubling and tripling parts of the STORC system to achieve UV light generation.

In this contribution, we performed two separate data acquisition campaigns: (1) the MSI of the 1.5×2 -mm area with 10- μm gaps between ablation craters and (2) depth profiling campaign within specified areas—microfossil-rich zone and a host mineral (quartz) area. The MSI campaign yielded 30,000 (150×200 pixels) mass spectra, where every pixel represents a histogram of 200 single laser shot spectra. The output mass spectra were processed using a single mass unit spectral decomposition (extraction of consecutive mass peak areas, following the footsteps of Meyer et al., 2017). Overall, 182 single mass unit intensities, retrieved from every pixel, were used to form the isotope intensity maps. Further, the Gaussian process (Kriging) interpolation was used to increase the resolution of the output maps by a factor of 2. In total, ²⁸Si, ¹⁶O, ¹²C, and ¹H maps were calculated to visualize the distribution of microfossils and filling quartz mineral on the surface of the sample. The second data acquisition campaign was performed to remove the organic contamination layer present on the surface and probe the original chemical composition of the microfossils and subsequently build a binary classification model. The depth profiling campaign resulted in the acquisition of 38,500 spectra from 15 depth profiles acquired from the microfossils-rich zone and a host mineral (see the supporting information for detailed information about data processing and filtering). The output spectral intensity profiles from both locations were log-transformed and z-score standardized.

The PCA of the depth profiling dataset was conducted using the correlation matrix computed on centered data. The first three principal components were extracted from the depth profiling dataset. The weighted correlation networks of inclusions present in the depth profiles were calculated using the direct Pearson pairwise correlation scores of 182 single unit mass intensities. The correlation scores retrieval resulted in the acquisition of 16,380 Pearson correlation pairs for given inclusion. Further, extracted correlation pairs were used as weights defined on pairwise edges in the construction of the undirected network. The force-directed layout (ForceAtlas2) provided with Gephi^{48,49} was used to visualize the network structure. The edge weight threshold was implemented to remove the insignificant correlation values from the network (see further down in the text). The pairwise kernel density estimates of biorelevant ratios and element intensities were used to visualize the density distributions of investigated locations (silicified host mineral and microfossils). Furthermore, 24 binary classification ML models (including classification trees, support vector machines, and ensemble models) were scored using the Matlab ML presets (see supporting information for more details). The isotope ratios and synthetic metrics (e.g., geometric mean values of light masses) were added to the ML dataset, making 196 variables in total. The fivefold cross-validation was used to avoid overfitting of the dataset. Within best-performing models, an additional 30-step Bayesian optimization (search through different learning hyperparameters) procedure was implemented to test for potential improvements in the output performance. For a more detailed description of ML models, information on PCA, and weighted correlation networks, we refer to the supporting information.

3 | RESULTS AND DISCUSSION

3.1 | LIMS imaging and depth profiling

All experimental measurement procedures—surface imaging and depth profiling—performed on the sample with a miniature LIMS system are schematically illustrated in Figure 1. The drawing is out of scale and intended to give a better understanding of the subject of this study. The distribution of microfossils embedded in a quartz matrix is shown with gray lenticular structures. Most of the preserved species studied by nano-microscopy are hollow and represent partially collapsed cell walls. An approximate estimate of the thickness of the cell walls mentioned in the figure is 500 nm; however, actual thicknesses are varying. For detailed morphological studies of these microfossils, we refer to literature.^{35,39} The small layer on the surface represents surface contamination with recent organic material. A focused UV-258-nm fs laser beam shown in Figure 1 was used to ablate and ionize material from the Gunflint chert. The produced ions were transmitted into a miniature TOF-MS (LIMS) developed for the operation on planetary surfaces.

To acquire information on the chemical composition of the stromatolitic layering from the Gunflint chert sample, we performed MSI of an area of a thin section containing two morphological features: (1) dense population of microfossils and (2) clean host mineral area. We identified a rectangular area (1.5 mm × 2 mm) (Figure 2A,B) where these features were present. To accurately sample the area under investigation, a 10- μ m gap between the ablation craters was chosen for the imaging, resulting in a grid with 30,000 ablation spots (with a single mass spectrum corresponding to each spot—see Figures 5 and S3–S5). To avoid material displacement and crater-to-crater cross-contamination from the ablation processes, a pulse train of 200 laser pulses was applied to each location, yielding a single mass spectrum. Because imaging implies probing material from different parts of the sample with different light absorption properties, suitable pulse energies were determined on preliminary craters from various locations prior to the imaging. Laser pulses with an energy of 0.36 [μ J] per pulse (measured at the sample surface) were found to be appropriate for both the dense microfossil assemblage and the clean host area. The diameter of the analytical spot was determined to be around 4–5 μ m for the imaging campaign within dominantly quartz locations and 7–8 μ m within microfossils.

Figure 2D,E shows the distribution of ¹H and ¹²C signal intensities on the surface of the Gunflint sample, extracted from the mass spectra using Simpson integration (details about integration procedure can be found in literature⁵⁰) and defined as an output current registered from the detector per unit of time (\log_{10} electrons * ns⁻¹). As is clear from Figure 2D,E, hydrogen and carbon are spatially correlated with the location of the microfossils identified by the optical microscopy (see Figure 2B). Resolution of the imaging reached a single cell level (see Figures S4 and S5) and could be improved by a factor of 2 in future campaigns without any analytical interference. Figure 2F,G displays the distribution of ²⁸Si and ¹⁶O intensities recorded on the surface of the sample. Both isotopes show a relatively homogeneous distribution, with a good correlation to each other. The host material in which the microfossils are embedded is diagenetic quartz with varying crystal sizes. It is also possible to observe an enhanced signal of ²⁸Si and ¹⁶O within the microfossil's lamination area due to the enhanced absorption of light by microfossils. Imaging of minor and trace elements was not

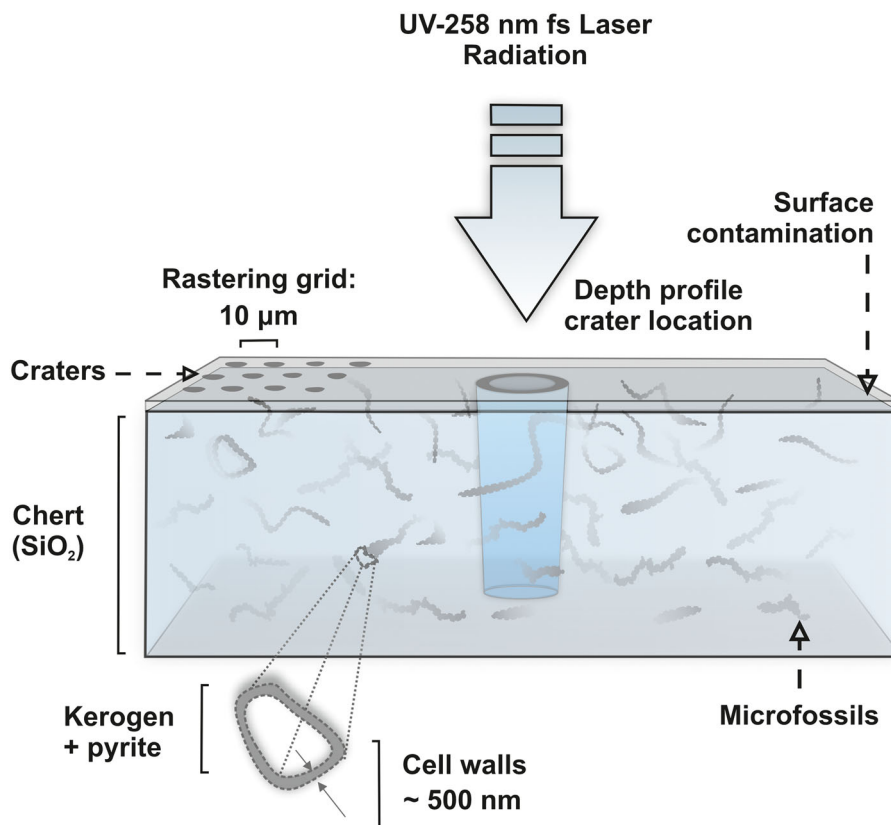


FIGURE 1 Schematic representation of the sample with three-dimensional distribution of various microfossils within the chert. The arrow represents focused fs laser light forming an ablation crater. The blue cylinder represents an ablation crater, formed during the depth profiling (not to scale). On the left side of the arrow, smaller ablation craters from the surface imaging are present (ablation craters are at different scales). On the bottom, the schematic composition of the hollow microfossils and approximate thickness of the cell walls are shown

possible due to isobaric contamination by hydrocarbon clusters in the mass spectra (see Figure S12). The separate depth profiling campaign was performed to remove the contaminated layer on the surface and probe the original chemical composition of the microfossils and host area.

3.2 | Depth profiling

Figure 3 shows the locations at which depth profiles were measured within the lamination area containing the population of microfossils and the host quartz area. Depth profiling analysis was conducted on nine spots containing microfossils and six spots of clean host quartz. Spots studied by depth profiling are independent of the grid that was used for MSI. For seven spots from the microfossils and six spots from the host area, 2500 spectra were measured simultaneously on two acquisition cards and summed together (forming a 5000-spectra dataset for a single depth profile before summation), where each spectrum consists of 200 single laser pulse spectra and corresponds to the single ablation layer. Two additional spots on a microfossil-rich area were measured with reduced histogramming down to 64, and 32 single laser shot spectra, in an attempt to obtain an even finer sampling of the microfossils. In total, 3000 spectra were collected from each of these spots (6000 spectra before preprocessing). A data extraction procedure is performed, retrieving intensities of the single mass units, utilizing direct Simpson integration⁵⁰ of the time-of-flight windows determined for each mass. In total, 182 single unit masses from each spectrum have been retrieved, including a background signal (noise measurements), which were determined in the time-of-flight window, free of any ion signal.

Figure 3A,B displays location and morphology of exemplary craters acquired during the depth profiling campaign. The dark patches in Figure 3B represent an aggregation of microfossils, where an arrow indicates location of the single lenticular microfossil. Figure 3C shows variation of the ¹²C mass peak intensities measured at the selected location. As is clear from Figure 3C, the ¹²C mass peak intensity measured within 32,500 spectra reveals clear intensity separation

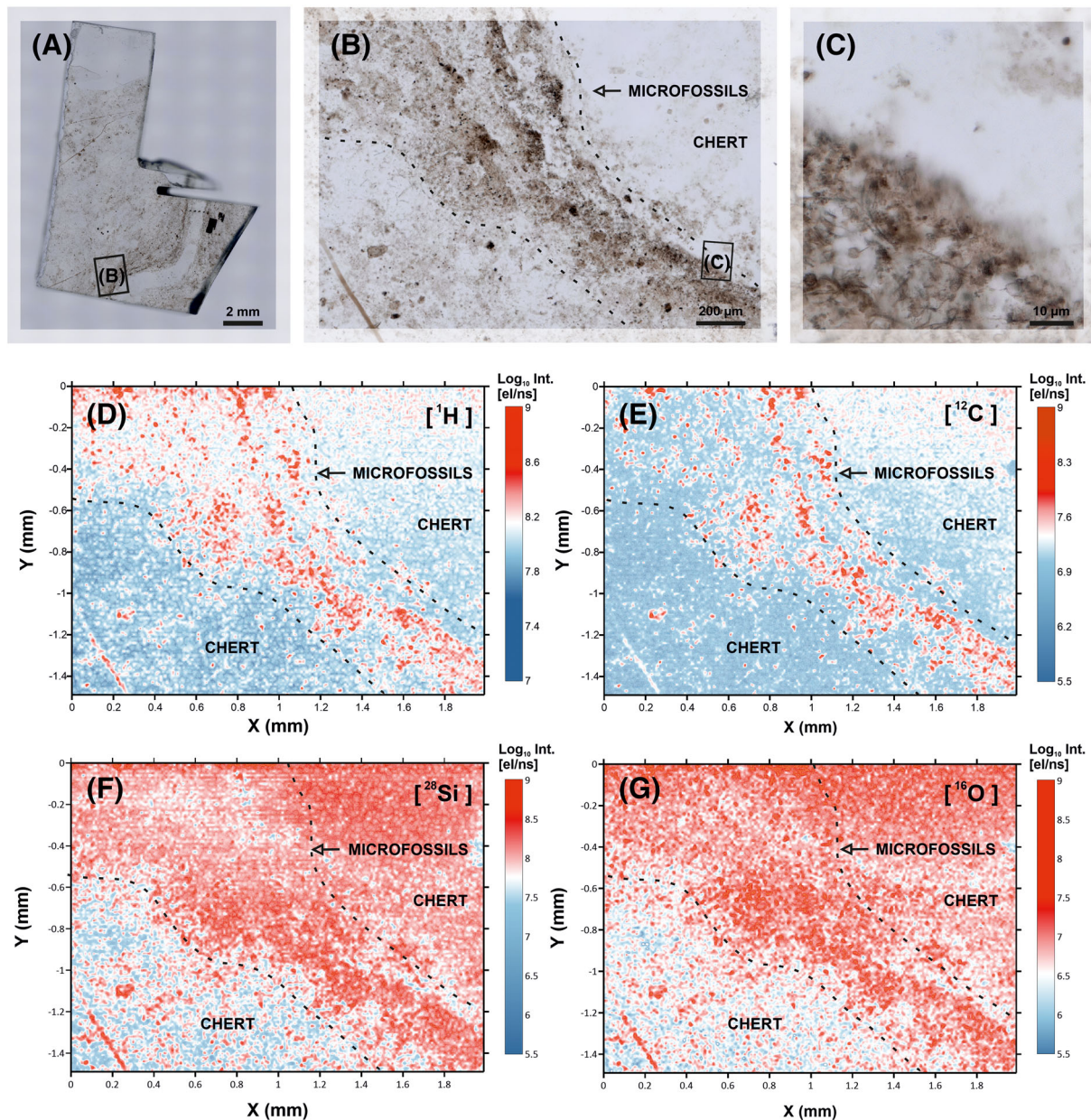


FIGURE 2 Optical images of the Gunflint thin section and results of the MSI. (A) Panoramic picture of the Gunflint thin section sample with a designated location of the area chosen for the MSI. (B) Image of the area chosen for the MSI with a designated location of the close-up picture (images are constructed by stacking of multiple focal points). The actual distribution of microfossils exposed to the surface is less dense but follows the same structure. (C) Close-up image of the distribution of microfossils within a densely populated area at the edge of the lamination. (D, E) Intensity maps of the ^1H and ^{12}C . Red areas correspond to the intense signal from the microfossils, and blue areas to the lower intensities from the surrounding chert. Black dashed line outlines the edge of the lamination area. To compare with the optical image of the same area, see Figure 2B. Lower panels (F) and (G): Intensity maps of ^{28}Si and ^{16}O , which constitutes inorganic silicified host of the Gunflint sample

boundary between two locations (note that intensities are presented in the log scale). A limited amount of ^{12}C signal, registered from the host region, may originate from the surface of the sample due to the widening of the crater, while ablation is progressing. Figure 3D shows the single depth profile from the microfossil-rich location and reveals increased ^{12}C intensities within specific depth regions, indicating that the measured carbon originates from the inclusions (Figure 3D, bars with location X and Y). In contrast, the depth profiles registered from the host region (Figure 3C) show the presence of a significantly reduced amount of carbon, in comparison with the depth profile acquired from the microfossil-rich lamination area. Localized aggregation of intense peaks of carbon within the bulk of the quartz matrix

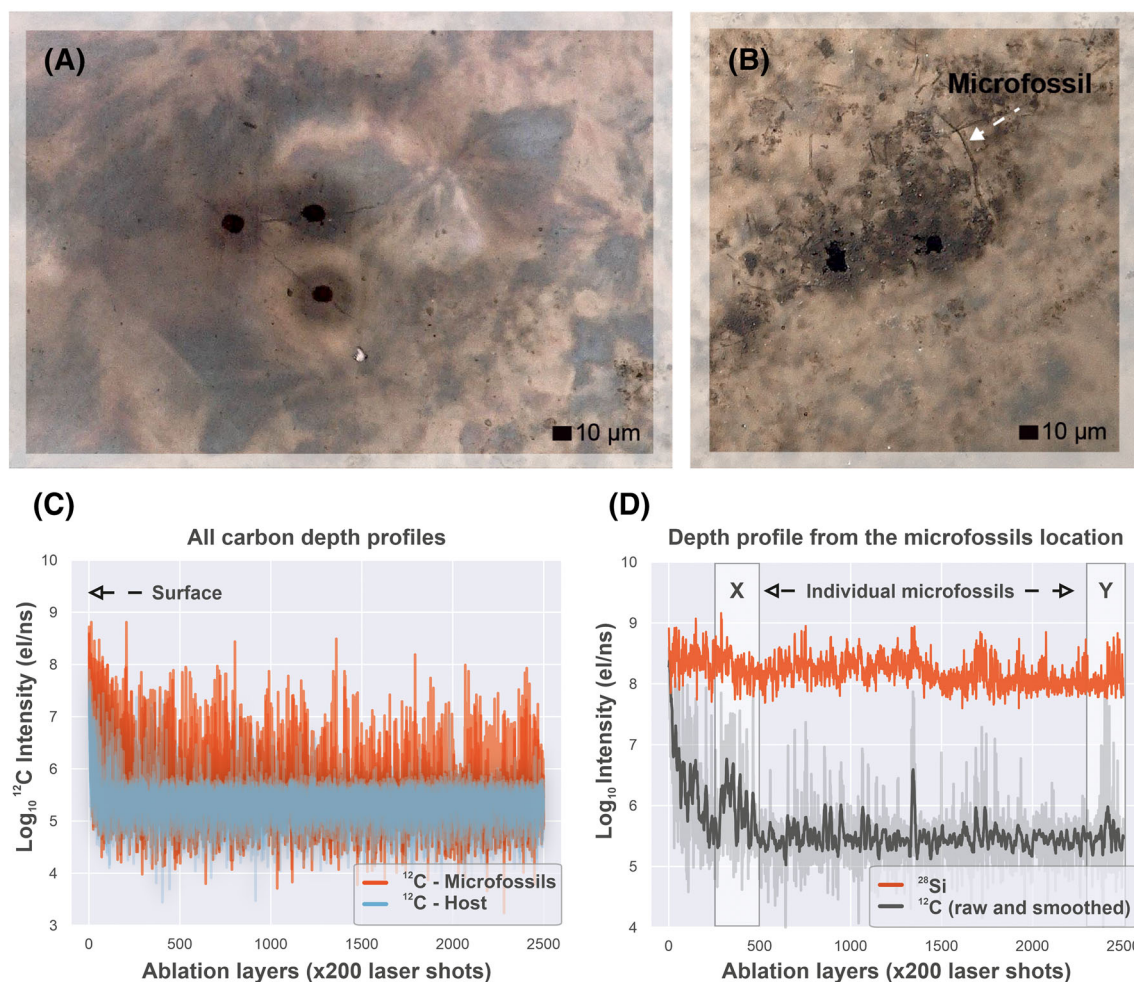


FIGURE 3 Location of the exemplary craters from the depth profiling campaign and registered ion yields from different locations. (A) Exemplary depth profile craters from the host area. (B) Exemplary depth profile craters from the microfossil aggregation zone. Arrow indicates location and relative size of the microfossil in comparison with the size of the analyzed crater. (C) Ion yield curves registered from the depth profiles. Superimposed ^{12}C depth profiles (integrated ^{12}C peak intensity) from the seven microfossil locations (orange line) and six host locations (blue line) (32,500 spectra in total) are shown. An intense carbon signal on the surface indicates the presence of surface contamination. (D) Single depth profile registered from the microfossil-rich spot (see Figure 3B). The ^{28}Si (orange line), ^{12}C (gray line—raw data, black—smoothed by moving average ^{12}C ion yield curve) depth profile constructed by extracting peak areas from 2500 consecutive spectra. Location of individual microfossils within the depth profile indicated by X and Y

is interpreted to be individual bodies of microfossils (see the sketch—Figure 1). Moreover, carbon-enriched inclusions are associated with other biorelevant elements: CHNOPS (see further in the text and Figure 4B,C), which indicates that these inclusions are indeed individual microfossils, located in the distinct depth regions. However, to prove that these localized spectra are acquired from a single source (microfossil), we calculated the correlation networks, which will be presented later in the text. Here, we need to mention that LIMS, being a destructive method, provides sensitive and spatially resolved measurements that are hard to achieve using bulk characterization methods. For example, in the low-biomass simulation of Martian sediments,^{10,11} the results have shown that LIMS can identify spatially constrained biosignatures in Mars analog environments.

Figure 4 shows spectra measured from different mineralogical inclusions present within the Gunflint subsurface. The spectrum measured at the host area (Figure 4A) reveals the chemical composition corresponding to the diagenetic quartz. Intense peaks of Si and O are readily recognized. Additionally, peaks of H, C, Na, K, and chain of SiO clusters can be identified in the spectrum (Figure 4A). The mass spectrum in Figure 4B was measured within location X (Figure 3D) at depth position 250–500. The spectrum reveals the complex chemical composition of the microfossil body intermixed with the host chemistry. The chemical composition measured within this spot represents a mixture of the

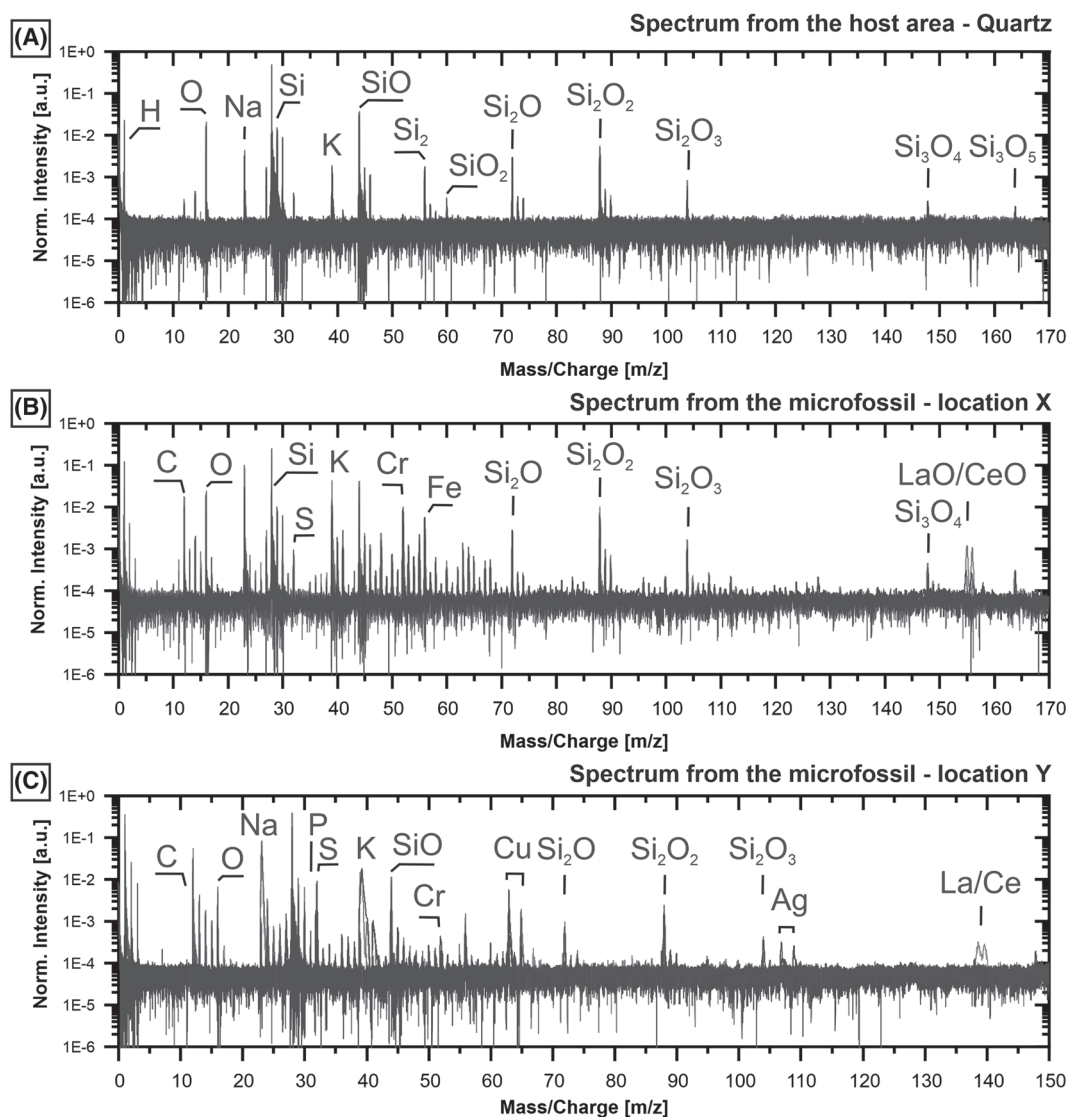


FIGURE 4 Mass spectra from various parts of the sample. (A) Mass spectrum from the host area. (B) Mass spectra from the microfossil (location X in the depth profile; see Figure 3D). (C) Mass spectrum from the microfossil (location Y in the depth profile; see Figure 3D). Note the increased peak intensities of biorelevant elements (CHNOPS) and richer chemistry within microfossils in comparison with the host mineral (quartz; see Figure 4A)

quartz mineral, kerogen from microfossil cell walls, and a polymetallic inclusion associated with the microfossil. Intense mass peaks of transition metals, Ti, Mn, Fe, and Cu, can be identified in the spectrum with a major contribution from Cr and additional minor contribution from La and Ce monoxides. The presence of kerogen is identified from the detection of C, H, N, O, P, and S. Additionally, multiple low-intensity C_xH_y compounds can be identified in the spectrum.

Figure 4C shows the mass spectrum measured at depth locations 2350–2500 (location Y; see Figure 3D) and reveals a different composition compared with the inclusion described above. In addition to the mass peaks registered from quartz and CHNOPS, there are also peaks of Mg, Al, K, Ca, Cr, Mn, La, and Ce, and mass peaks of Cu and Ag could be noted. The latter are rather unexpected to be found within microfossils because they are known to be elements with high cytotoxicity (i.e., they are toxic to cells).

Although LIMS can yield sensitive measurements of elements and isotopes, it can be challenging to determine mineralogical composition of multiple microinclusions (smaller than the size of the probing laser spot). The pairwise correlation factors between single mass unit intensities are calculated in an attempt to identify mineralogical composition of investigated inclusions. Figure 5 shows two networks calculated from the individual microfossils (Figure 3D) and

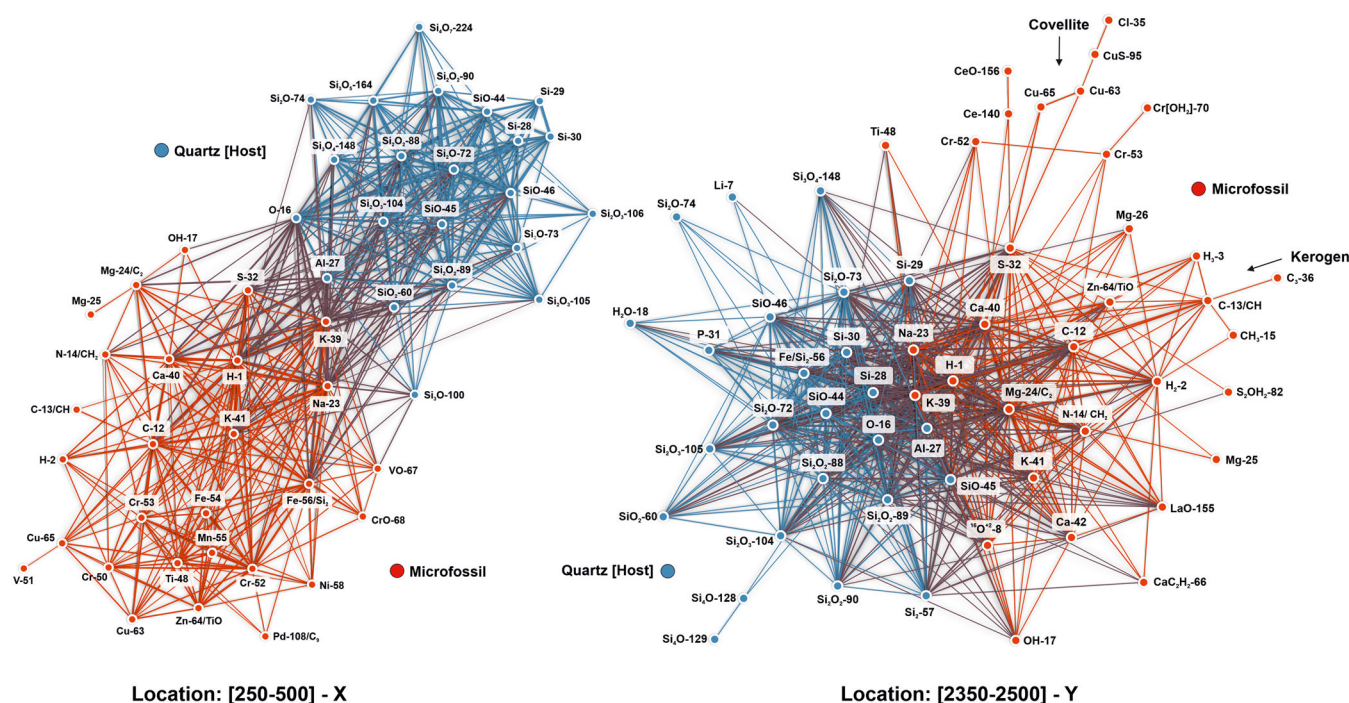


FIGURE 5 Weighted mass correlation networks calculated from the inclusions registered at locations X and Y (see Figures 3D and 4B, C). Left: Network from the location X (see Figures 3D and 4B) (ρ larger than 0.4). The network shows presence of two separate entities within studied location—microfossil (red nodes) and quartz (blue nodes). Right: Network from the depth location Y (see Figures 3D and 4C) (ρ larger than 0.2). The network shows two separate inclusions—microfossil (red nodes) and quartz (blue nodes). Chemical composition and topology of network X are different from network Y, which could be attribute to the different size and chemical composition of microfossils. The straight line between two nodes (single unit masses— m/z) represents a linear correlation factor measured within the microscopic inclusions. The node colors are assigned according to the Louvain modularity score. Note the central elements within each subgroup—C, H are among central elements within microfossils and silicon oxides within quartz

visualized using an open-source graph drawing platform Gephi.⁴⁹ The mass correlation network shown on the left side was calculated from location X, which is located at the depth region: 250–500. Correlation factors (ρ) larger than 0.4 were used to visualize only strongly correlated masses (see full correlation matrices in the supporting information). Node colors are chosen according to the modularity rank,⁵¹ calculated from the network topology (modularity Q is a parameter that measures the density of links in the graph inside communities as compared with links between communities). Blue nodes correspond to the elements registered from the quartz mineral, whereas red nodes represent elements and isotopes registered from the microfossil body. Clear separation of the inclusion from the host chemistry could be observed within this network—host mineral (quartz) colored with blue nodes and a microfossil (red nodes).

The mass correlation network shown on the right side of Figure 5 was calculated from the depth region 2350–2500, at location Y (see Figure 3D), and represents the chemical composition of another microfossil. Due to the lower number of spectra registered from this inclusion (size of the inclusion was considerably smaller than the inclusion described above), the ρ cutoff value was set to 0.2. However, even with low correlation factors, it is possible to obtain the appropriate modularity ranks and to increase the interpretability of the data. Within the analyzed microscopic inclusion, S is interconnected with Cu, implying the presence of covellite within the body of the microfossil (see Figure 5, location Y, top red nodes), or closely attached to it. P measured in the microfossil is more interconnected with the host (quartz) elements (left blue node in network Y). This observation can be attributed to the “shouldering” effect of the intense ^{30}Si peak, which affects the integration window of P, thus modifying its ρ value and positioning in the graph. One notable feature of this correlation network is that by identifying the least and most interconnected nodes, it is possible to find predictive masses that are unique for each of the given mineralogical classes. The topology of the correlation networks also reveals a centrality measure, which indicates the importance of the element in a network. We can see that in Figure 5 left, there are some elements that are present both within the quartz and a microfossil—H, Na, K, O—these nodes could be characterized with high betweenness centrality.⁵⁶Fe is also among the central elements in a network, due to the presence of the isobaric contribution of Si_2 . Analyzing the microfossil-related network separately (only red

nodes), one can see that ^{12}C , ^1H , ^{41}K , ^{54}Fe are among the central isotopes, which also reflects the importance of this isotope in the chemical composition of the microfossil bodies. Any organic matter preserved within the bulk of the host mineral requires the existence of such networks with measurable centrality of C and H and a separate modularity rank. Depending on the chemical integrity (state of decay) of the inclusions, better preserved microfossils also have better connectivity and higher covariance, whereas finely dispersed carbon incorporated into the body of the matrix will not have such metrics and likely to be located within the outer nodes of the network.

The co-occurrence of P, Ce, and La (Figure 4B,C) within studied locations is indicative of the presence of the monazite microscopic inclusion. There are two possible interpretations for the presence of REEs in association with the microfossils: first is the intracellular incorporation and passive mineralization of La and Ce by living organisms and, second, postmortem mineralization (secondary incorporation of these elements). However, because La and Ce have been measured within our dataset only in association with microfossils, intracellular incorporation seems more plausible. The connection of Fe with S (Figure 5 left) indicates the presence of pyrite, which was described as a byproduct of the metabolic activity of sulfate-reducing microbes.³⁵ However, localization of metallic nodes in the lower part of the network indicated presence of the third inclusion, which likely represents Cr-rich nodule with impurities of Fe, Mn, Cu, and Ti (see bottom red nodes in Figure 5, location X). The complex chemical composition associated with some of the microfossils might also be indicative of the development of tolerance to the polymetallic toxicity. For example, Cu, registered at location Y, is an essential trace element for aerobic organisms; however, Cu might be lethal to microbes if homeostasis is not maintained.⁵² Cr has also been reported as a highly toxic and mutagenic element for bacterial colonies.⁵³ The C and H bearing microfossils reveal close association with Na, K, Mg, Ca also with Fe and S. Overall, analysis of the inclusions from the depth profiles reveals a complex chemical composition indicating presence of chemically distinct microfossils with identifiable hydrothermal mineralization patterns (presence of typical hydrothermal elements like Cu, Fe, and Ag).

3.3 | Identification of empirical biosignatures

As it was shown in Figures 2, 4, and 5, carbon and hydrogen peak intensities are correlated with the location of the microfossils, and within our sample, carbon might be used as a tracer of the microfossils. The full depth profiling dataset sampled from the microfossil-rich locations was divided into host and microfossil data by thresholding the carbon signal. Depth profiles from the microfossil locations were sorted using a threshold of $5.8 \log_{10} \text{ el/ns}$ (higher than the noise level) to create a subset of data that represent only microfossil-related spectra, assuming that the C signal originates from the microfossils. The depth profiling dataset was additionally filtered to the depth region 500–2500 within both locations (host mineral area or aggregation of microfossils), to avoid contribution from the surface data. In total, after filtering, we formed a dataset with 12,000 spectra from the host location and 1454 spectra from the microfossil-rich location. Figure 6 presents kernel density estimates (two-dimensional density maps) calculated for two specific regions and represents a probability distribution function of element intensities for two groups: quartz and microfossils (i.e., inorganic or bioorganic intensity regions). Figure 6A–D represents the variation of the signal from the microfossils plotted against the same mass intensities measured from the host region—red kernels are calculated from the microfossil-rich location, and blue kernels from the host area (see Figure 3A,B). Multiple non-overlapping intensity regions associated with the microfossils could be observed. These intensity regions can serve as predictive borderlines for the identification of the organic remnants from other Gunflint-like cherts. In contrast, Figure 6E–G represents the variation of the elements associated with the inorganic host, shows mostly overlapping intensities, and indicates that most of the spectra from the microfossils have a significant contribution from the quartz mineral. Figure 6F shows that the Fe signal registered from the microfossils interferes with the Si_2 molecule, and significant parts of it protrude into the higher Fe content area, indicating increased Fe content within the microfossil bodies. Figure 6H displays a perfectly overlapping variation of the Gaussian background signal derived from the two locations.

Figure 7A shows partially overlapping clusters of $^1\text{H}/^{12}\text{C}$ and $^{16}\text{O}/^{12}\text{C}$ ratios measured from the host (blue kernels) and the microfossils (red and orange kernels). Because most of the microfossils are hollow³⁹ (see Figure 1) and smaller than the LIMS analytical spot size, they will be sampled with the encapsulating host mineral. In addition to the chemical composition of the microfossils, compositional details of the host mineral are likely to be registered. Hence, intensity values of ^1H and ^{16}O , formerly occurring within microfossils, are interfering with the same isotopes from the quartz mineral; hence, they can be subtracted. The results of these corrections are shown in Figure 7A,B with orange kernels. As can be seen from this figure, the locations of the kernels from the microfossils coincide with empirically determined

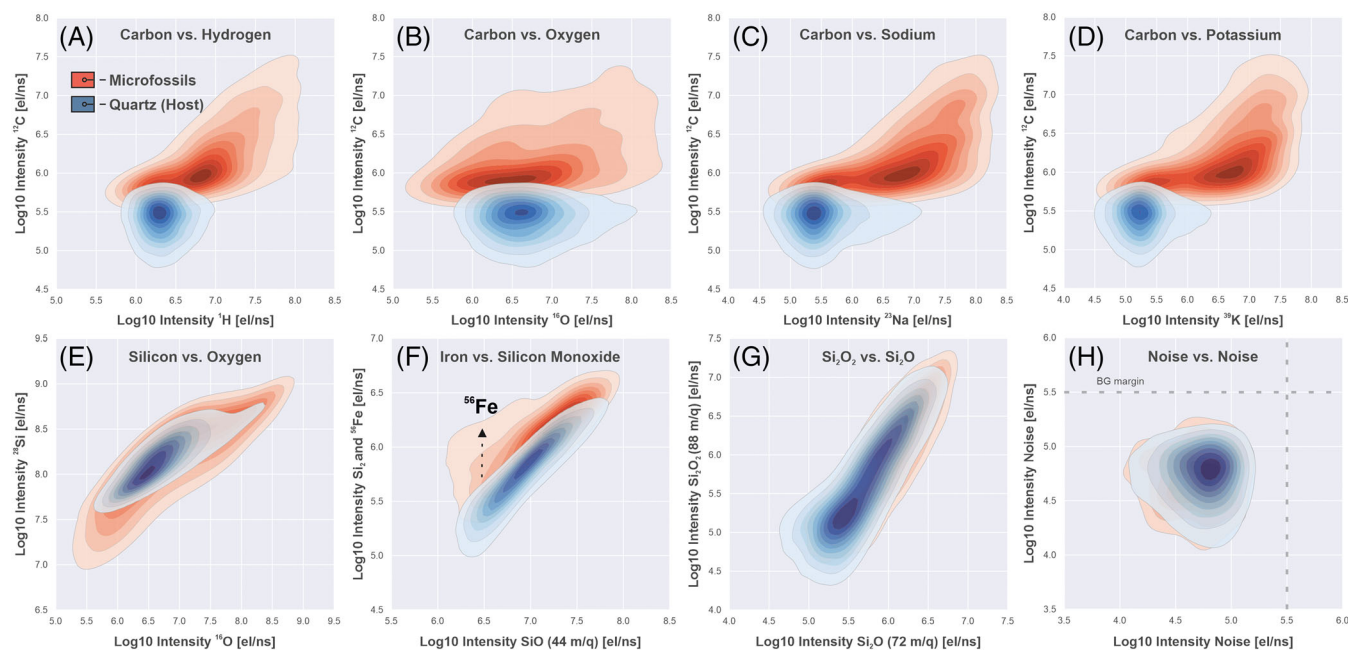


FIGURE 6 Kernel density estimates (KDE) of m/z intensities for two groups: Red kernels are calculated from the measurements performed within the microfossil-rich locations. A total of 13,454 spectra shown within each plot (1454 spectra measured from microfossil-rich location). Blue kernels are calculated from the measurements acquired from the host locations (12,000 spectra). (A)–(D) represent the total variation of C, H, O, Na, and K signal measured within microfossils and host locations. (E)–(G) represent the total variation of Si, O, Si_2 (^{56}Fe), Si_2O , and Si_2O_2 signal intensities measured from the inorganic host (quartz) and microfossil-rich locations. (H) A total variation of the noise signal; dashed line outlines conservative background margin

regions of organic compounds (lipids, peptides, sugars, and condensed hydrocarbons [kerogen]). The identification of ratio boundaries for different organic compounds was demonstrated in the literature using ultra-high-resolution mass spectrometry.^{54,55} Black boxes shown in Figure 7A schematically represent the location of those boundaries. Empirically determined shapes of the complex organic compounds are derived at overlapping areas and typically have more complex shapes to those presented on the plot.

Data collected from the densely populated microfossil area (Figure 7A red and orange kernels) hint at the presence of lipid and peptide signatures, which aligns with the previously reported identification of amides from the Gunflint microfossils and exceptional preservation capacity of cherts.^{34,37,56} However, they likely represent a mixing ratio between the original kerogen and quartz ratios. A fraction of the data also intrudes into the area of kerogens, which can be classified as a Kerogen Type I (Algal).⁵⁷ However, there is a part of the red kernels that overlap with the host mineral data as well. Data collected from the host area contain mostly quartz mineral, and most of the measured ratios represent signal-to-noise ratios of ^{16}O and ^1H , due to the low concentration of ^{12}C within analyzed depth profiles from the host locations. The results presented in Figure 7A indicate that organic hydrocarbons measured at the Gunflint sample are significantly reduced in ^{16}O and relatively saturated in ^1H (increased abundance of ^1H). A shift of the $^1\text{H}/^{12}\text{C}$ values towards relative ^1H saturation (mentioned in the plot as hydrogenation) can also be promoted by the different optical absorption of the laser energy. Different absorption rates might shift the total energy balance for ablation and ionization of the microfossils, consecutively resulting in a more efficient release of ^1H ions. Whereas a significant part of the ablated and ionized material can also be expected to represent a mixture of the signal from the microfossils and quartz mineral (due to the effective diameter of the focused laser), and it might be challenging to subtract the contribution of the isobaric input from the quartz entirely. Figure 7B, similarly to the Van Krevelen plot (Figure 7A), represents bivariate distribution of $^{28}\text{Si}/^{12}\text{C}$ and $^{16}\text{O}/^{12}\text{C}$ values and indicates presence of the separate ratio space characteristic of microfossils. The same correction procedure as in Figure 7A has been applied for $^{16}\text{O}/^{12}\text{C}$ distribution, which is shown with orange kernels.

Figure 7C,D shows the distribution of PCA values obtained from the two distinct groups—measurements from the host area in contrast to the measurements from the microfossil-rich zone (12,863 spectra in total). Spectra from the microfossil location could be separated from the spectra collected within the host area, except for a small number,

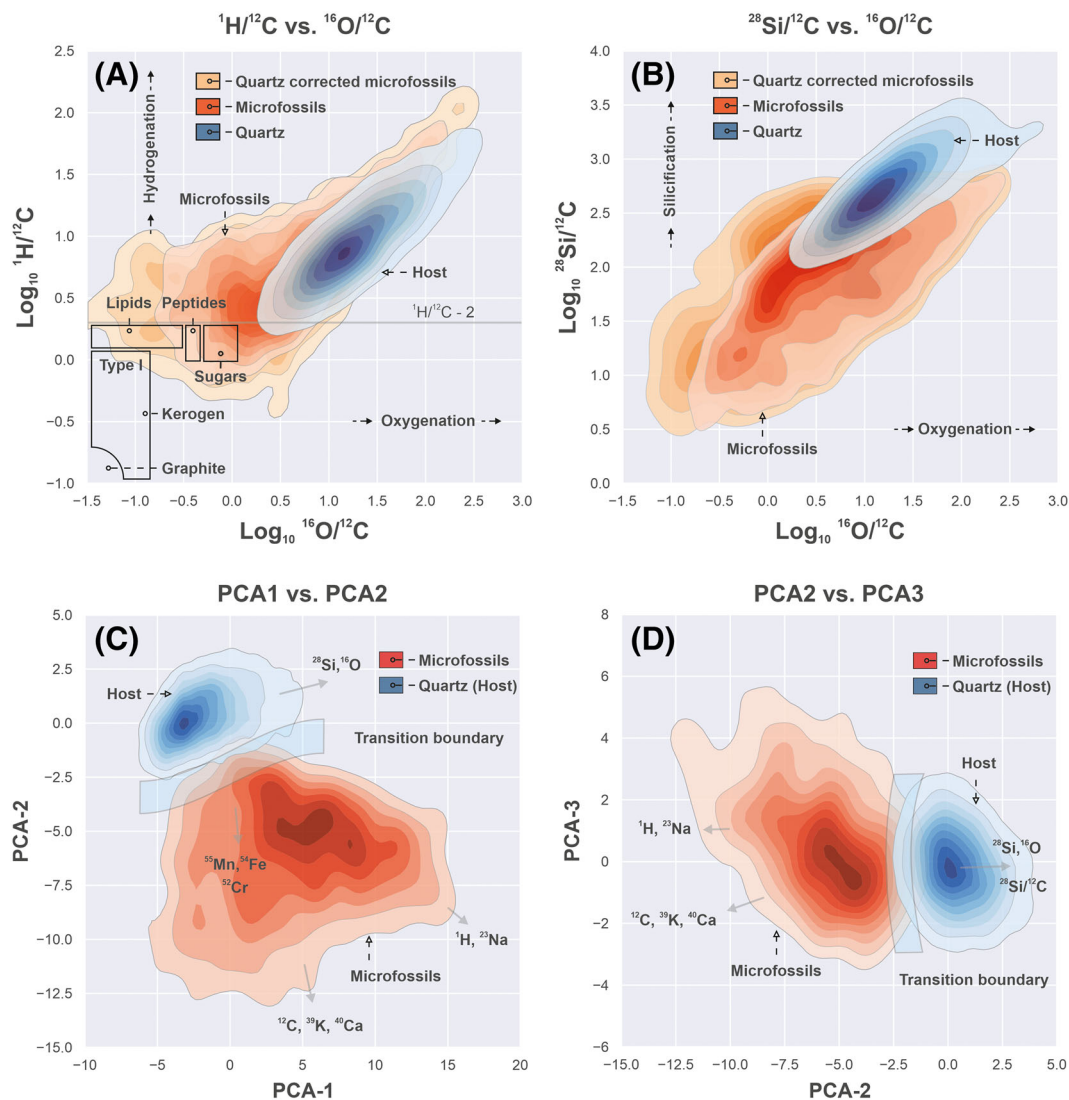


FIGURE 7 (A) Kernel density estimates (KDE) of $^1\text{H}/^{12}\text{C}$ and $^{16}\text{O}/^{12}\text{C}$ ratios (Van Krevelen plot). Blue kernels represent values measured from the host area. Red kernels show the distribution of $^1\text{H}/^{12}\text{C}$ and $^{16}\text{O}/^{12}\text{C}$ values calculated from the area densely populated with microfossils. Orange kernels represent the same data, as in red kernels, but corrected for ^1H and ^{16}O interfering signal, registered from the co-occurring with microfossils quartz mineral (details about correction procedure described further in the text). Black bars: Schematic representation of the boundaries of lipids, peptides, sugars, and kerogen within the Van Krevelen space (values are taken from the literature^{45–47}). (B) Kernel density estimates (KDE) of $^{28}\text{Si}/^{12}\text{C}$ and $^{16}\text{O}/^{12}\text{C}$ ratios. Blue kernels represent values measured from the host area. Red kernels show the distribution of $^{28}\text{Si}/^{12}\text{C}$ and $^{16}\text{O}/^{12}\text{C}$ values measured from the area densely populated with microfossils. Orange kernels represent the same data, as in red kernels, but corrected for ^{16}O interfering signal, registered from the co-occurring with microfossils quartz mineral. (C and D) 2D projections of the 196 features into the principal components space. Blue kernels represent data from the host locations. Red kernels represent data collected from the microfossil-rich zone. Arrows schematically represent loading directions for different single unit masses. The blue transparent line indicates the location of the transition boundary between two classes. Among 196 features, 179 are normalized intensities (z-scores) of single unit masses, 15 features are normalized (z-scores) element ratios, and two last features are z-scores of averaged intensities of light masses (1–74 m/z) and geometrical mean values for light masses (1–74 m/z)

which interferes with the host measurements. To increase the separability of the dataset, we further thresholded C intensities to 6 log_{10} el/ns (see supporting information), which reduced the microfossils dataset from 1454 spectra to 863 spectra. We schematically identified the transition boundary with a light blue transparent line, which shows the location of the estimated transition boundary between the inorganic host (quartz) spectra and spectra from the microfossils. The transition of one class into another could be explained by the ablation of the small portions of the microfossils (nm thick cell walls in the bulk of the host mineral). The thickness of the rims of the collapsed cell walls reported from the Gunflint microfossils varies from the tens of nm³⁹ to first micrometers,³⁵ which might explain statistically

more prevalent low-intensity regions in KDE plots (Figures 6 and 7). Figure 7C,D indicates that intermediate levels between classes are sampled when spectra from one class gradually turn into the spectra from the other class. It is worth noting that even with only the first two principal components, a clear separation between two main classes can be seen. Additionally, as was demonstrated before (Figures 4B,C and 5), and noting the dispersion of the PCA loadings, it is possible to identify that there are potentially more than one class of microfossils within the Gunflint dataset. A significant part of the dataset is clustered within the dark red areas, representing the majority of simple kerogen containing microfossils. However, we could see from Figure 7C that kernels protrude from the hydrocarbon saturated area towards areas with notable metallic content, pointing towards the presence of uptake of Fe, Mn, and Cr. This observation agrees with the results reported previously on the diversity of the microbiome within Gunflint waters. Cyanobacteria were proposed to be a dominant part of the Gunflint stromatolites^{31,40,58}; however, other interpretations are possible. Presence of Mg in the spectra (Figures 4B,C and 5) can indicate the presence of degradation products of chlorophyll, because all chlorophyll molecules share chlorin magnesium ligand in their structure, supporting the photosynthetic hypothesis. A community of saprophytic heterotrophs was proposed as part of the microbiome,³⁵ which are assumed to have a different set of metallic catalysts and enzymes, hence, identifiable chemical fingerprints. Nevertheless, clear separation of the chemically distinct subclasses of microfossils requires even higher statistics and linkage to the morphological features.

Overall, the broad set of mass spectrometric characteristics, measured from the Gunflint microfossils, can be identified using the full feature space, with the ML classification models (see Table S1). By applying an ensemble classification algorithm (adaptive boosting), we achieved a 99.7% separation rate between classes: inorganic host (quartz) or organic inclusions (microfossils). A small subset of misclassifications is attributed to the transition boundary line, where spectra are protruding from the host region towards microfossils. By extracting the 196 features from the single mass spectra, we created 19,110 unique sets of mass and ratio pairs, in which two classes might be separated (i.e., C vs. H, and C vs. O). It is possible to achieve a full separation score of 100% by further limiting the C intensities; however, this will affect the quality of the learned borderlines between classes. Such models, containing the empirical biosignatures from the known terrestrial samples with a proven biogenic origin, might be used as a deployable solution onboard of the Martian rovers, providing an additional line of evidence towards establishing the biogenicity of a given putative sample by assessing the proximity of the data to the spectra acquired from the Gunflint and/or other model samples. However, future work will be required to identify the capacity of LIMS system for distinguishing between true biological organic material (life) as opposed to organic material that was produced non-biologically, for example, via Fischer-Tropsch-Type (FTT) synthesis.

4 | CONCLUSION

In summary, the chemical composition of Precambrian microfossils from the 1.88-Ga Gunflint Formation was investigated using a laser-based miniature TOF-MS. Locations of microfossils were identified on the surface of the sample utilizing MSI. The composition of individual microfossils embedded within the chert was identified using depth profiling and single mass unit spectral decomposition. Utilizing MSI, weighted mass correlation networks, isotopic ratios, and projection of intensities into the low dimension using PCA, it was demonstrated that the microfossils, and associated with them mineralization, have a unique chemical composition that could be identified from the LIMS microprobe data. High-throughput LIMS imaging combined with depth profiling has been shown to be capable of yielding new insights into the distribution, preservation, and elemental speciation of the microfossils in Precambrian cherts.

ACKNOWLEDGMENTS

The authors would like to acknowledge the financial support from the Swiss National Science Foundation. DW acknowledges funding from the Australian Research Council via a Future Fellowship Grant.

CONFLICT OF INTEREST

No competing interests exist.

PEER REVIEW

The peer review history for this article is available at <https://publons.com/publon/10.1002/cem.3370>.

DATA AVAILABILITY STATEMENT

The data that support the findings of this study are available from the corresponding author upon reasonable request.

ORCID

Rustam A. Lukmanov  <https://orcid.org/0000-0001-9257-7410>

Andreas Riedo  <https://orcid.org/0000-0001-9007-5791>

REFERENCES

1. McMahon S, Bosak T, Grotzinger JP, et al. *A Field Guide to Finding Fossils on Mars*. Hoboken, New Jersey: John Wiley & Sons, Ltd; 2018:1012-1040.
2. Westall F, Foucher F, Bost N, et al. Biosignatures on Mars: what, where, and how? Implications for the search for Martian life. *Astrobiology*. 2015;15(11):998-1029.
3. Vago JL, Westall F, Pasteur Instrument Teams, Landing S, et al. Habitability on early Mars and the search for biosignatures with the ExoMars rover. *Astrobiology*. 2017;17(6-7):471-510.
4. Orosei R, Lauro SE, Pettinelli E, et al. Radar evidence of subglacial liquid water on Mars. *Science*. 2018;361(6401):490-493.
5. Grotzinger JP, Sumner DY, Kah LC, et al. A habitable fluvio-lacustrine environment at Yellowknife Bay, Gale Crater, Mars. *Science*. 2014;343(6169):1242777.
6. Navarro-González R, Navarro KF, de la Rosa J, et al. The limitations on organic detection in Mars-like soils by thermal volatilization-gas chromatography-MS and their implications for the Viking results. *Proc Natl Acad Sci U S A*. 2006;103(44):16089-16094.
7. Wurz P, Abplanalp D, Tulej M, et al. Mass spectrometric analysis in planetary science: investigation of the surface and the atmosphere. *Sol Syst Res*. 2012;46(6):408-422.
8. Hofmann BA. Morphological biosignatures from subsurface environments: recognition on planetary missions. *Space Sci Rev*. 2008;135(1-4):245-254.
9. Brasier MD, Wacey D. Fossils and astrobiology: new protocols for cell evolution in deep time. *Int J Astrobiol*. 2012;11(4):217-228.
10. Stevens AH, McDonald A, de Koning C, et al. Detectability of biosignatures in a low-biomass simulation of martian sediments. *Sci Rep*. 2019;9(1):9706.
11. Riedo A, de Koning C, Stevens AH, et al. The detection of elemental signatures of microbes in martian mudstone analogs using high spatial resolution laser ablation ionization mass spectrometry. *Astrobiology*. 2020;20(10):1224-1235.
12. Wiesendanger R, Wacey D, Tulej M, et al. Chemical and optical identification of micrometer-sized 1.9 billion-year-old fossils by combining a miniature laser ablation ionization mass spectrometry system with an optical microscope. *Astrobiology*. 2018;18(8):1071-1080.
13. Veneranda M, Lopez-Reyes G, Manrique-Martinez JA, et al. ExoMars Raman laser spectrometer (RLS): development of chemometric tools to classify ultramafic igneous rocks on Mars. *Sci Rep*. 2020;10:1-14.
14. Smith JP, Smith FC, Booksh KS. Spatial and spectral resolution of carbonaceous material from hematite (α -Fe₂O₃) using multivariate curve resolution-alternating least squares (MCR-ALS) with Raman microspectroscopic mapping: implications for the search for life on Mars. *Analyst*. 2017;142(17):3140-3156.
15. Smith JP, Smith FC, Booksh KS. Multivariate curve resolution-alternating least squares (MCR-ALS) with Raman imaging applied to lunar meteorites. *Appl Spectrosc*. 2018;72(3):404-419.
16. Konstantinidis M, Lalla EA, Daly MG, et al. Elemental estimation of terrestrial analogues from the CanMars rover field campaign using LiRS: implications for detecting silica-rich deposits on Mars. *Icarus*. 2021;358:114113-114124.
17. Manrique-Martinez JA, Lopez-Reyes G, Alvarez-Perez A, et al. Evaluation of multivariate analyses and data fusion between Raman and laser-induced breakdown spectroscopy in binary mixtures and its potential for solar system exploration. *J Raman Spectrosc*. 2020;51(9):1702-1717.
18. Ligterink NFW, Grimaudo V, Moreno-García P, et al. ORIGIN: a novel and compact laser desorption-mass spectrometry system for sensitive in situ detection of amino acids on extraterrestrial surfaces. *Sci Rep*. 2020;10(1):9641.
19. Grimaudo V, Tulej M, Riedo A, et al. UV post-ionization laser ablation ionization mass spectrometry for improved nm-depth profiling resolution on Cr/Ni reference standard. *Rapid Commun Mass Spectrom*. 2020;34:e8803.
20. Riedo A, Grimaudo V, Moreno-García P, et al. Laser ablation/ionisation mass spectrometry: sensitive and quantitative chemical depth profiling of solid materials. *Chimia*. 2016;70(4):268-273.
21. Riedo A, Bieler A, Neuland M, Tulej M, Wurz P. Performance evaluation of a miniature laser ablation time-of-flight mass spectrometer designed for in situ investigations in planetary space research. *J Mass Spectrom*. 2013;48(1):1-15.
22. Wiesendanger R, Tulej M, Riedo A, Frey S, Shea H, Wurz P. Improved detection sensitivity for heavy trace elements using a miniature laser ablation ionisation mass spectrometer. *J Anal At Spectrom*. 2017;32(11):2182-2188.
23. Tulej M, Riedo A, Neuland MB, et al. CAMAM: a miniature laser ablation ionisation mass spectrometer and microscope-camera system for in situ investigation of the composition and morphology of extraterrestrial materials. *Geostand Geoanal Res*. 2014;38(4):441-466.
24. Goesmann F, Brinckerhoff WB, Raulin F, et al. The Mars Organic Molecule Analyzer (MOMA) instrument: characterization of organic material in martian sediments. *Astrobiology*. 2017;17(6-7):655-685.
25. Li X, Danell RM, Pinnick VT, et al. Mars Organic Molecule Analyzer (MOMA) laser desorption/ionization source design and performance characterization. *Int J Mass Spectrom*. 2017;422:177-187.

26. Brioso C, Thissen R, Thirkell L, et al. Orbitrap mass analyser for in situ characterisation of planetary environments: performance evaluation of a laboratory prototype. *Planet Space Sci.* 2016;131:33-45.
27. Selliez L, Brioso C, Carrasco N, et al. Identification of organic molecules with a laboratory prototype based on the Laser Ablation-CosmOrbitrap. *Planet Space Sci.* 2019;170:42-51.
28. Arevalo R Jr, Selliez L, Brioso C, et al. An Orbitrap-based laser desorption/ablation mass spectrometer designed for spaceflight. *Rapid Commun Mass Spectrom.* 2018;32(21):1875-1886.
29. Tulej M, Neubeck A, Ivarsson M, et al. Chemical composition of micrometer-sized filaments in an aragonite host by a miniature laser ablation/ionization mass spectrometer. *Astrobiology.* 2015;15(8):669-682.
30. Neuland MB, Grimaudo V, Mezger K, et al. Quantitative measurement of the chemical composition of geological standards with a miniature laser ablation/ionization mass spectrometer designed for in situ application in space research. *Meas Sci Technol.* 2016;27(3):035904.
31. Barghoorn ES, Tyler SA. Microorganisms from the Gunflint chert: these structurally preserved Precambrian fossils from Ontario are the most ancient organisms known. *Science.* 1965;147(3658):563-575.
32. Awramik SM, Semikhatov MA. The relationship between morphology, microstructure, and microbiota in three vertically intergrading stromatolites from the Gunflint Iron Formation. *Can J Earth Sci.* 1979;16(3):484-495.
33. Cloud PE. Significance of the Gunflint (Precambrian) microflora. *Science.* 1965;148:563-575.
34. Alleon J, Bernard S, Le Guillou C, et al. Molecular preservation of 1.88 Ga Gunflint organic microfossils as a function of temperature and mineralogy. *Nat Commun.* 2017;7:11977.
35. Wacey D, McLoughlin N, Kilburn MR, et al. Nanoscale analysis of pyritized microfossils reveals differential heterotrophic consumption in the ~1.9-Ga Gunflint chert. *PNAS.* 2013;110:1053-1060.
36. Cady SL, Skok JR, Gulick VG, Berger JA, Hinman NW. Siliceous hot spring deposits: why they remain key astrobiological targets. In: *From Habitability to Life on Mars.* Amsterdam, Netherlands: Elsevier; 2018:179-210.
37. Alleon J, Bernard S, le Guillou C, et al. Early entombment within silica minimizes the molecular degradation of microorganisms during advanced diagenesis. *Chem Geol.* 2016;437:98-108.
38. Schelble RT, Westall F, Allen CC. ~1.8 Ga iron-mineralized microbiota from the Gunflint Iron Formation, Ontario, Canada: implications for Mars. *Adv Space Res.* 2004;33:1268-1273.
39. Lepot K, Addad A, Knoll AH, et al. Iron minerals within specific microfossil morphospecies of the 1.88 Ga Gunflint Formation. *Nat Commun.* 2017;8(1):1-11. <https://doi.org/10.1038/ncomms14890>
40. Awramik SM, Barghoorn ES. The Gunflint microbiota. *Precambrian Res.* 1977;5(2):121-142.
41. House CH, Schopf JW, McKeegan KD, Coath CD, Harrison TM, Stetter KO. Carbon isotopic composition of individual Precambrian microfossils. *Geology.* 2000;28(8):707-710.
42. Javaux EJ, Lepot K. The Paleoproterozoic fossil record: implications for the evolution of the biosphere during Earth's middle-age. *Earth Sci Rev.* 2017;176:68-86.
43. Azov VA, Mueller L, Makarov AA. Laser ionization mass spectrometry at 55: Quo Vadis? *Mass Spectrom Rev.* 2020. <https://doi.org/10.1002/mas.21669>
44. Tulej M, Ligterink NFW, de Koning C, et al. Current progress in femtosecond laser ablation/ionisation time-of-flight mass spectrometry. *Applied Sciences.* 2021;11(6):2562.
45. Riedo A, Meyer S, Heredia B, et al. Highly accurate isotope composition measurements by a miniature laser ablation mass spectrometer designed for in situ investigations on planetary surfaces. *Planet Space Sci.* 2013;87:1-13.
46. Riedo A, Tulej M, Rohner U, Wurz P. High-speed microstrip multi-anode multichannel plate detector system. *Rev Sci Instrum.* 2017; 88(4):045114.
47. Moreno-García P, Grimaudo V, Riedo A, Tulej M, Wurz P, Broekmann P. Towards matrix-free femtosecond-laser desorption mass spectrometry for in situ space research. *Rapid Commun Mass Spectrom.* 2016;30(8):1031-1036.
48. Bastian M, Heymann S, Jacomy M. Gephi: an open source software for exploring and manipulating networks. In: *Proceedings of the International AAAI Conference on Web and Social Media.* Palo Alto, California: Association for the Advancement of Artificial Intelligence (AAAI); 2009.
49. Jacomy M, Venturini T, Heymann S, Bastian M. ForceAtlas2, a continuous graph layout algorithm for handy network visualization designed for the Gephi software. *PLoS ONE.* 2014;9(6):e98679.
50. Meyer S, Riedo A, Neuland MB, Tulej M, Wurz P. Fully automatic and precise data analysis developed for time-of-flight mass spectrometry. *J Mass Spectrom.* 2017;52(9):580-590.
51. Blondel VD, Guillaume J-L, Lambiotte R, Lefebvre E. Fast unfolding of communities in large networks. *J Stat Mech: Theory Exp.* 2008; 2008(10):P10008.
52. Ladomersky E, Petris MJ. Copper tolerance and virulence in bacteria. *Metallomics.* 2015;7(6):957-964.
53. Viti C, Marchi E, Decorosi F, Giovannetti L. Molecular mechanisms of Cr(VI) resistance in bacteria and fungi. *FEMS Microbiol Rev.* 2014;38(4):633-659.
54. Brockman SA, Roden EV, Hegeman AD. Van Krevelen diagram visualization of high resolution-mass spectrometry metabolomics data with OpenVanKrevelen. *Metabolomics.* 2018;14(4):48-53.
55. Kim S, Kramer RW, Hatcher PG. Graphical method for analysis of ultrahigh-resolution broadband mass spectra of natural organic matter, the Van Krevelen diagram. *Anal Chem.* 2003;75(20):5336-5344.

56. Alleon J, Bernard S, Le Guillou C, et al. Organic molecular heterogeneities can withstand diagenesis. *Sci Rep.* 2017;7:1508.
57. Hutton A, Bharati S, Robl T. Chemical and petrographic classification of kerogen/macerals. *Energy Fuel.* 1994;8(6):1478-1488.
58. Boal D, Ng R. Shape analysis of filamentous Precambrian microfossils and modern cyanobacteria. *Paleobiology.* 2010;36(518):555-572.

SUPPORTING INFORMATION

Additional supporting information may be found in the online version of the article at the publisher's website.

How to cite this article: Lukmanov RA, Tulej M, Ligterink NFW, et al. Chemical identification of microfossils from the 1.88-Ga Gunflint chert: Towards empirical biosignatures using laser ablation ionization mass spectrometer. *Journal of Chemometrics.* 2021;e3370. doi:10.1002/cem.3370